AGU PUBLICATIONS

JGR

Journal of Geophysical Research: Space Physics

RESEARCH ARTICLE

10.1002/2016JA022930

Key Points:
- The induced AWs have stronger localized impacts, and GWs sustain much longer in the IT
- The wave-wave interactions contribute up to 3% of the perturbations
- Event-induced TEC perturbations can be isolated with proper modeling efforts

Correspondence to:
C. Y. Lin,
incen@vt.edu

Citation:
Lin, C. Y., Y. Deng, C. Sheng, and D. P. Drob (2017), A study of the nonlinear response of the upper atmosphere to episodic and stochastic acoustic-gravity wave forcing, *J. Geophys. Res. Space Physics*, *122*, doi:10.1002/2016JA022930.

Received 11 MAY 2016
Accepted 3 JAN 2017
Accepted article online 7 JAN 2017

A study of the nonlinear response of the upper atmosphere to episodic and stochastic acoustic-gravity wave forcing

Cissi Y. Lin[1], Yue Deng[1], Cheng Sheng[2], and Douglas P. Drob[3]

[1]Department of Physics, University of Texas at Arlington, Arlington, Texas, USA, [2]High Altitude Observatory, National Center for Atmospheric Research, Boulder, Colorado, USA, [3]Naval Research Laboratory, Washington, DC, USA

Abstract Perturbations caused by geophysical and anthropogenic events on the ground have been observed to propagate upward and impact the upper atmosphere. Gravity waves with wavelengths less than 750 km are known to be responsible for the total electron content (TEC) perturbations and to play a significant role in the mass, momentum, and energy budgets of the mesosphere and lower thermosphere. These waves are, however, difficult to continuously measure, globally resolve, and deterministically specify in first-principle ionosphere-thermosphere (IT) models. In this study, we investigate IT response to induced acoustic-gravity waves resulting from strong time-varying lower atmospheric wave forcing, including a traveling wave packet (TWP) and stochastic gravity wave (SGW) fields using the nonlinear Global Ionosphere Thermosphere Model (GITM) with high-resolution grids of 0.08° in longitude and latitude. When TWP and SGW forcing occurs concurrently, the induced gravity waves (GWs) cause variation of ±8.8% in neutral, ±6.2% in electron density, and ±1.5% in TEC. The magnitudes decrease by 2.4% (from ±8.8% to ±6.4%) with the SGW effects simulated separately and subtracted; importantly, interactions between TWP and SGW contribute to ±1.4% of the perturbations. On the other hand, the induced acoustic waves (AWs) cause variation of ±13.9% in neutral, ±2.1% in electron density, and ±0.4% in TEC. Furthermore, GWs sustain tens of minutes after the TWP has passed through the lower atmosphere and clear traveling ionospheric disturbances and traveling atmospheric disturbances are developed. We demonstrate that clear wave structures from an episodic event can be isolated even under a ubiquitously and overwhelmingly perturbed atmosphere.

1. Introduction

Waves of various spatial and temporal scales, including acoustic waves (AWs), gravity waves (GWs), tides, and planetary waves, modify the dynamics of the terrestrial atmosphere at all altitudes. Perturbations caused by geophysical and anthropogenic events on the ground have been observed propagating upward and impacting the ionospheric electron density, including volcano eruptions [*Dautermann et al.*, 2009a, 2009b], earthquakes [*Liu et al.*, 2001], tsunami [*Galvan et al.*, 2011, 2012; *Meng et al.*, 2015; *Occhipinti et al.*, 2006; *Saito et al.*, 2011; *Tsugawa et al.*, 2011], strong tropospheric circulation (often referred as “deep convection”) [*Nishioka et al.*, 2013; *Perwitasari et al.*, 2015; *Yue et al.*, 2014], explosions [*Calais et al.*, 1998], and even space shuttle launches [*Bowling et al.*, 2013; *Calais and Minster*, 1996].

While many first-principle numerical modeling efforts have been devoted to study atmospheric waves in the upper atmosphere, a fully 3-D coupling from the ground to the ionosphere and thermosphere (IT) has not yet been achieved to span extensive ranges in spatial, temporal, and frequency domains. For example, among the upward propagating waves, propagation of the acoustic-gravity waves (AGW) is particularly sensitive to small-scale structures of the background atmosphere [*Heale and Snively*, 2015; *Hedlin and Drob*, 2014]. Currently, the fine-structured waves (wavelength shorter than 100 km) are poorly measured especially at the altitudes above 100 km and are computationally challenging for most models to incorporate properly. The global circulation models (GCMs) developed at the National Center of Atmospheric Research (NCAR) have a standard resolution of 5° in longitude by 5° in latitude and can be modified to 2.5° by 2.5° [*Hagan et al.*, 2007; *Liu et al.*, 2013], which is sufficient for studies of large-scale planetary waves and tides but insufficient to resolve waves with horizontal wavelengths less than 100 km. A mesoscale-resolving GCM using the NCAR WACCM (Whole Atmosphere Community Climate Model) has been used to study GWs [*Liu et al.*, 2014], but due to its configuration the results are presently limited—only up to the lower thermosphere (~150 km), which is well below the ionosphere’s *F* region.

On the other hand, theoretical wave modeling efforts have been devoted to intensively study the propagation of AGWs from the lower atmosphere to the upper atmosphere [*Broutman et al.*, 2003, 2006, 2009, 2014; *Frances*, 1973; *Hickey et al.*, 1997, 2009, 2010; *Hines*, 1960, 1967, 1968a, 1968b; *Pitteway and Hines*, 1963; *Vadas and Fritts*, 2005; *Vadas and Nicolls*, 2012; *Vadas et al.*, 2015; *Yeh and Liu*, 1974, references therein]. In the recent years, with an analytical, linear, compressible solutions for 3-D inviscid fluid for determining GW, it is shown that including compressibility in the GW modeling is necessary for high-frequency, medium-scale wave packets [*Vadas*, 2013]. The numerical full-wave model [*Hickey et al.*, 1997] solving the linear, compressible, 1-D equations for a single frequency and wave number has been expended to solving for a spectrum of GWs [*Hickey et al*., 2009]. The 2-D nonlinear and compressible model of *Snively* [2013, and references therein] has been used recently for studies of acoustic and gravity waves generated by vertical forcing, and recently for gravity wave propagation and dissipation in the thermosphere by *Heale et al*. [2014]. Using its neutral atmospheric output to drive a self-consistent ionosphere model, *Zettergren and Snively* [2013, 2015] have also investigated the ionospheric response to acoustic waves generated by sources of different spatial and temporal scales. The necessity of including compressibility in the GW calculation without hydrostatic assumption is also demonstrated by the GCM results [*Deng et al*., 2008; *Deng and Ridley*, 2014]. Meanwhile, hemispheric coupling of the ionospheric response to lower atmospheric perturbations is observed in the SAMI3 (Sami3 is Also a Model of the Ionosphere) simulations [*Huba et al*., 2015]. Though providing great insights on AGW dynamics, many of the theoretical models are sometimes constrained in spatial domain (1-D or 2-D), under a steady state assumption, relying on parameterization to facilitate computational requirements, or lack of self-consistent two-way neutral-ion coupling to fully represent the true atmosphere.

To fully understand how AGWs generated in the lower atmosphere impact the IT system more realistically, we need a self-consistent 3-D IT model that is capable to trace neutral and ionized species, to account for ion-neutral coupling, and to resolve wave properties spatially and temporally. The Global Ionosphere Thermosphere Model (GITM) is such a model. It has flexible grid sizes, relaxes hydrostatic assumptions, and allows for nonhydrostatic solutions [*Ridley et al*., 2006; *Deng et al*., 2008]. The simulation time step is, in general, less than 2 s. A recent study has presented the hydrostatic and nonhydrostatic cutoff frequencies for vertically propagating waves and showed that certain high-frequency GWs with small horizontal scale may be reflected and ducted in nonhydrostatic models but propagating in hydrostatic models [*Deng and Ridley*, 2014]. Therefore, GITM is ideally suited for this study.

The main focus of this paper is to examine and to identify the effects from episodic and stochastic forcing and to provide quantitative analysis of the linear and nonlinear IT response to the superposition and interaction of waves in an inhomogeneous perturbed background atmosphere. We utilize GITM to examine the nonlinear IT response to induced AGWs by an episodic event with and without concurrent time-varying stochastic gravity wave (SGW) fields. The effects of superposition and interaction investigated in this paper include the residual components that result from interaction between different types of forcing and the background atmosphere during the differencing process and that cannot be completely subtracted off. The residual does not include exclusively wave-wave interactions though which could and are allowed to exist in the simulation. We select a traveling wave packet (TWP) to represent an episodic event because with the same magnitude of perturbation it carries greater energy compared to point-like sources and also resembles spatial and temporal features of tsunami wavefronts. GITM is used in previous work as a part of the tsunami-ionospheric coupling simulation [*Meng et al*., 2015], in which the assumptions are made that wavelength and frequency of a tsunami do not change when the induced waves propagate from sea level to 100 km, with magnitudes of perturbations following a simple *e*-fold rule without consideration of vertical variation of the background atmospheric conditions. In this study, we specify characteristics of the TWP, such as amplitude, wavelength, and group/phase speed, to resemble a strong tsunami source at GITM's lower boundary layers directly. The SGW model [*Drob et al*., 2013; *Hedlin and Drob*, 2014] specifies GW spectrum for the troposphere and ray-traces waves upward in spectral domain to the lower thermosphere accounting for winds, critical layer filtering, saturation, and attenuation where it is implemented to GITM. The implemented scales of forcing are carefully selected based on previous studies [*Meng et al*., 2015; *Warner and McIntyre*, 1996], and the magnitudes of IT perturbations are expected to be around 2% for TEC as in most of the observed cases [*Occhipinti et al*., 2006; *Saito et al*., 2011; *Tsugawa et al*., 2011] and 10% for the neutral density at general activity levels. We would like to emphasize that the main goal of the paper is to present the interactions between coherent forced waves and a stochastic wave background in the IT for the presented cases. This study aims to qualitatively and quantitatively investigate the consequences of such forcing and to serve as a critical step toward a better coupling from ground to upper atmosphere in a high-resolution GCM setting.

2. Model Description

2.1. Global Ionosphere Thermosphere Model (GITM)

GITM is a self-consistent 3-D IT model. With the advantages of flexible 3-D grid sizes and the ability to solve for nonhydrostatic solutions, GITM is ideal for studying wave dynamics in the IT system. It uses altitudinal grids rather than pressure grids as most GCMs do. GITM is developed incorporating modern concept of parallel computing to facilitate increasing computational demands of higher spatiotemporal resolution in upper atmospheric modeling.

GITM solves thermodynamic equations for multiple species in spherical coordinates. Vertical velocity is solved for each neutral species, *s*, while horizontal velocity is common for all. The vertical continuity equation is

$$\frac{\partial N_s^v}{\partial t} = -\frac{\partial u_{r,s}}{\partial r} - \frac{2u_{r,s}}{r} - u_{r,s}\frac{\partial N_s}{\partial t} \tag{1}$$

where N is density, u is radial velocity, r is radial distance, and t is time. The vertical momentum equation is

$$\begin{aligned}\frac{\partial u_{r,s}}{\partial t} + u_{r,s}\frac{\partial u_{r,s}}{\partial r} + \frac{u\theta}{r}\frac{\partial u_{r,s}}{\partial \theta} + \frac{u\phi}{r\cos\theta}\frac{\partial u_{r,s}}{\partial \phi} + \frac{k}{M_s}\frac{\partial T}{\partial r} + T\frac{k}{M_s}\frac{\partial N_s}{\partial r}\\ = g + F_s + \frac{u_\theta^2 + u_\phi^2}{r} + \cos^2(\theta)\Omega^2 r + 2\cos(\theta)\Omega u_\phi\end{aligned} \tag{2}$$

where θ is latitude, ϕ is longitude, k is Boltzmann constant, M is molecular mass, g is gravitational acceleration, Ω is angular velocity of Earth, and F is the forces due to ion-neutral and neutral-neutral friction in the vertical direction. The complete list of equations solved in GITM can be found in work by *Ridley et al.* [2006] and *Deng and Ridley* [2007].

In this study, GITM has been used to study the response of the IT system to fine-scale waves induced by different lower atmospheric source types, including individual and collective forcing from an episodic event and constantly present background wave activities. As stated in section 1, the horizontal wavelength of fine-scale structures in midfrequency GWs is about a few tens of kilometers (a fraction of 1°), usually beyond resolvable for most GCMs. As GITM has a flexible resolution and can run both globally and regionally, the simulation domain is set to be 9.6° by 9.6°, centered at (41.06°N, 247.14°E) as shown in Figure 1. The horizontal resolution is 0.08° by 0.08°. The altitude covers 100–600 km with vertical resolution of one third of the scale height, which is ~1.7 km at the lower boundary. According to Nyquist theorem, this setting equivalently provides the ability to resolve waves with horizontal wavelength of ~15 km and vertical wavelength of ~3.4 km at the lower thermosphere; the time step of less than 2 s potentially enables detection of waves with frequency up to 0.25 Hz (period shorter than 4 s). We acknowledge that it is important to sample waves higher than minimal requirement of Nyquist frequency to better resolve waves of interest. Therefore, the scales of the events presented in this study are selected accordingly. The episodic and stochastic forcing is implemented at the lower boundary, which is at ~98 km.

The simulation corresponds to the location of a previous wave propagation study considering a large acoustic event that occurs at the Utah Test and Training Range (UTTR) between 1 and 2 P.M. local time (20:00–21:00 UT) on 11 June 2007 [*Drob et al.*, 2013; *Hedlin and Drob*, 2014]. Solar activity was low on the day with the $F_{10.7}$ index of 74.20 and the 81 day average of 73.97. Geomagnetic activity was also low with the *Ap* index of 4. The local background profiles are shown in Figure 2. The horizontal magenta line indicates GITM's lower boundary, where the boundary conditions are specified: neutral species (shown as mass density) from the NRLMSISE-00 model [*Picone et al.*, 2002] (blue), electron number density from the IRI model [*Rawer et al.*, 1978 l; *Bilitza et al.*, 2011] (green), and neutral wind from the Horizontal Wind Model (HWM) model [*Drob et al.*, 2015] (red; solid for zonal wind and dotted for meridional wind). The GITM results are presented in black. The SGW model also uses Naval Research Laboratory Mass Spectrometer and Incoherent Scatter Radar (NRLMSIS) and HWM to specify the ambient atmosphere.

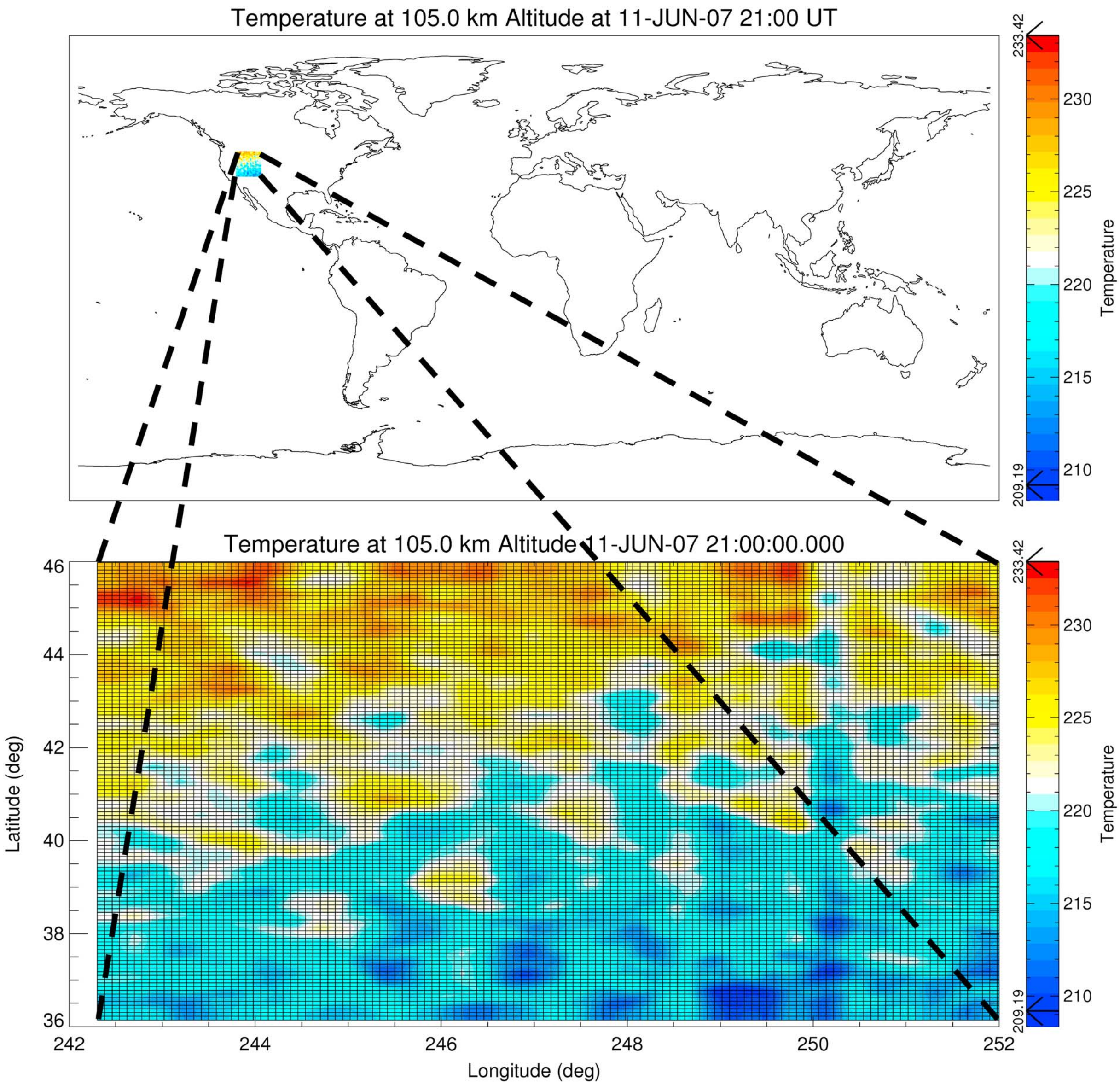

Figure 1. The simulation domain is 9.6° by 9.6°, centered at (41.06°N, 247.14°E). The horizontal resolution is 0.08° by 0.08°.

2.2. Stochastic Gravity Wavefield

The SGW model was developed to account for observed effects of the atmosphere's inherent GW spectrum on long-range AW propagation [*Drob et al*., 2013; *Hedlin and Drob*, 2014]. The SGW is a hybrid of earlier works by *Warner and McIntyre* [1996, 2001], *Broutman et al*. [2003, 2006, 2009], *Vadas and Fritts* [2005], and many others. The calculations start with an empirical GW spectrum in the upper troposphere, ray-trace the wave modes within the spectrum from ground sources upward into the thermosphere using the anelastic dispersion relation and including attenuation, apply parameterization for wave breaking and dissipation in the spectral domain, and give ground-to-space vertical profiles of the winds, temperature, density, molecular viscosity, etc. Using these perturbation GW fields in conjunction with range-dependent 2-D acoustic Parabolic Equation method and 3-D acoustic ray-trace calculations, as well as a frequency-dependent acoustic source function model, *Hedlin and Drob* [2014] show that inclusion of GW fluctuation fields is essential for explaining the observed phenomenology of infrasonic signal's arrival, amplitude, and duration from far-field sources. Inherited in *Hedlin and Drob*'s [2014] work, wave modes include five evenly spaced values of intrinsic

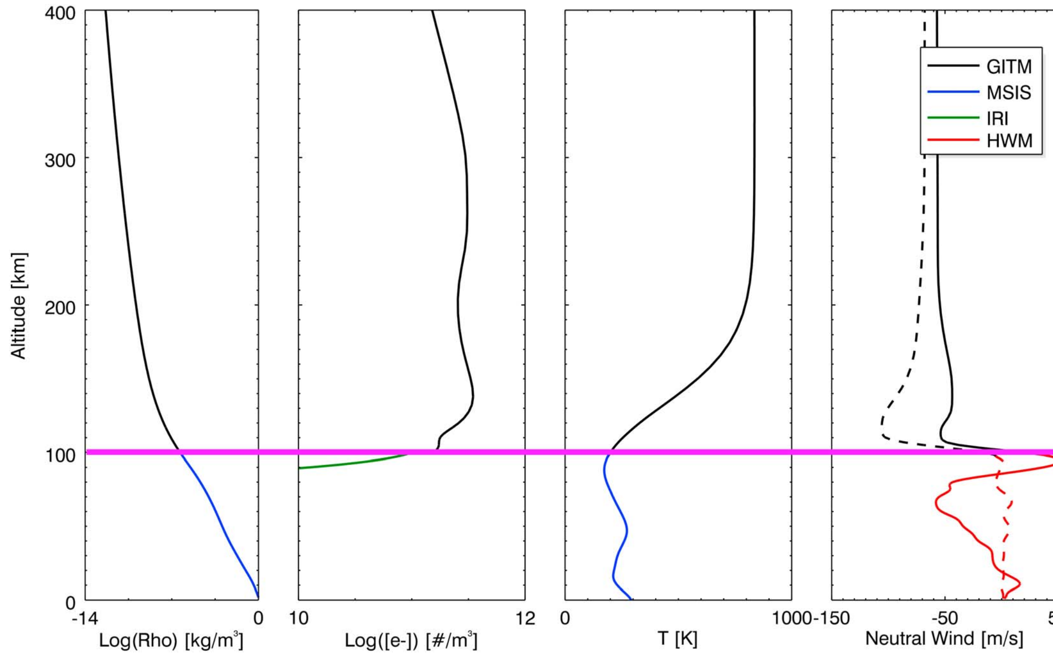

Figure 2. Altitudinal profiles of the background atmosphere (neutral mass density, electron number density, temperature, and neutral wind) at UTTR (41.06°N, 247.14°E) at 3 P.M. (local time) on 11 June 2007. The horizontal magenta line indicates the lower boundary of GITM, where the boundary conditions are specified: neutral species from the NRLMSIS model (blue), electron density from the IRI model (green), and neutral wind from the HWM model (red; solid for zonal wind and dotted for meridional wind). The GITM results are presented in black. The SGW model uses NRLMSIS and HWM to specify the ambient atmosphere.

frequency between $2f$ and $N/\sqrt{5}$, where f is the Coriolis frequency and N is the buoyancy frequency. In this paper we apply the SGW for an entirely different purpose.

The implemented SGW fields have a horizontal resolution of 8 km over a 1024 × 1024 km periodic domain and a vertical resolution of 200 m over the altitude range between 0 and 180 km. Figures 3a and 3c illustrate the SGW fields in zonal wind at altitude (Figure 3a) 170 km and (Figure 3c) 100 km. The horizontal grids in GITM are selected to incorporate the SGW fields. The SGW forcing is added onto the background wind at GITM's lower boundary ghost cells where the boundary condition is open. In general, the SGW includes trapped waves via a uniform approximation through the caustic regions. However, in order to be more physically self-consistent, these waves are turned off for the purposed of the present investigation. Only upward propagating waves are considered at the interface of the two models. Figures 3b and 3d show the differential fields (D2, as defined in Table 3, further discussion presented in section 3) in zonal wind from GITM at the same epoch, illustrating the effects of the SGW forcing. The GITM differential field in zonal wind at 100 km shown in Figure 3d is very similar to the SGW field as it is merely a grid above where the forcing is implemented. At 170 km, the developed wave patterns from GITM as shown in Figure 3b differ significantly from the SGW fields in Figure 3a. At 170 km, the magnitude of change in the SGW fields is close to ±25 m/s, whereas that in the GITM results is slightly greater than ±20 m/s, within 20%. The discrepancy in the wave pattern may be caused by multiple reasons. While GITM solves for 3-D thermodynamics equations for the IT species at each grid point, the SGW model considers only the neutral ambient atmosphere; employs various parameterization schemes, such as in viscous and thermal damping [*Drob et al.*, 2013], and does not consider chemistry, ion-neutral coupling, and wave-wave interactions. For molecular thermal conductivity, GITM adapts a simple parameterization [*Schunk and Nagy*, 2009] and SGW adapts the more complex and general form [*Banks and Kockarts*, 1973]. The key coefficient, K_m, in the two parameterization schemes differ by up to 20% depending on altitudes [*Semenov and Shved*, 2008], which could potentially contribute to an overall 5–10% difference in thermal conductivity calculations. This comparison illustrates the first main research result. GITM accounts for nonlinear effects of wave-wave interaction, feedback with the atmosphere, and other important dynamical mechanisms through the solution of the fully coupled multispecies fluid equations. Though beyond the

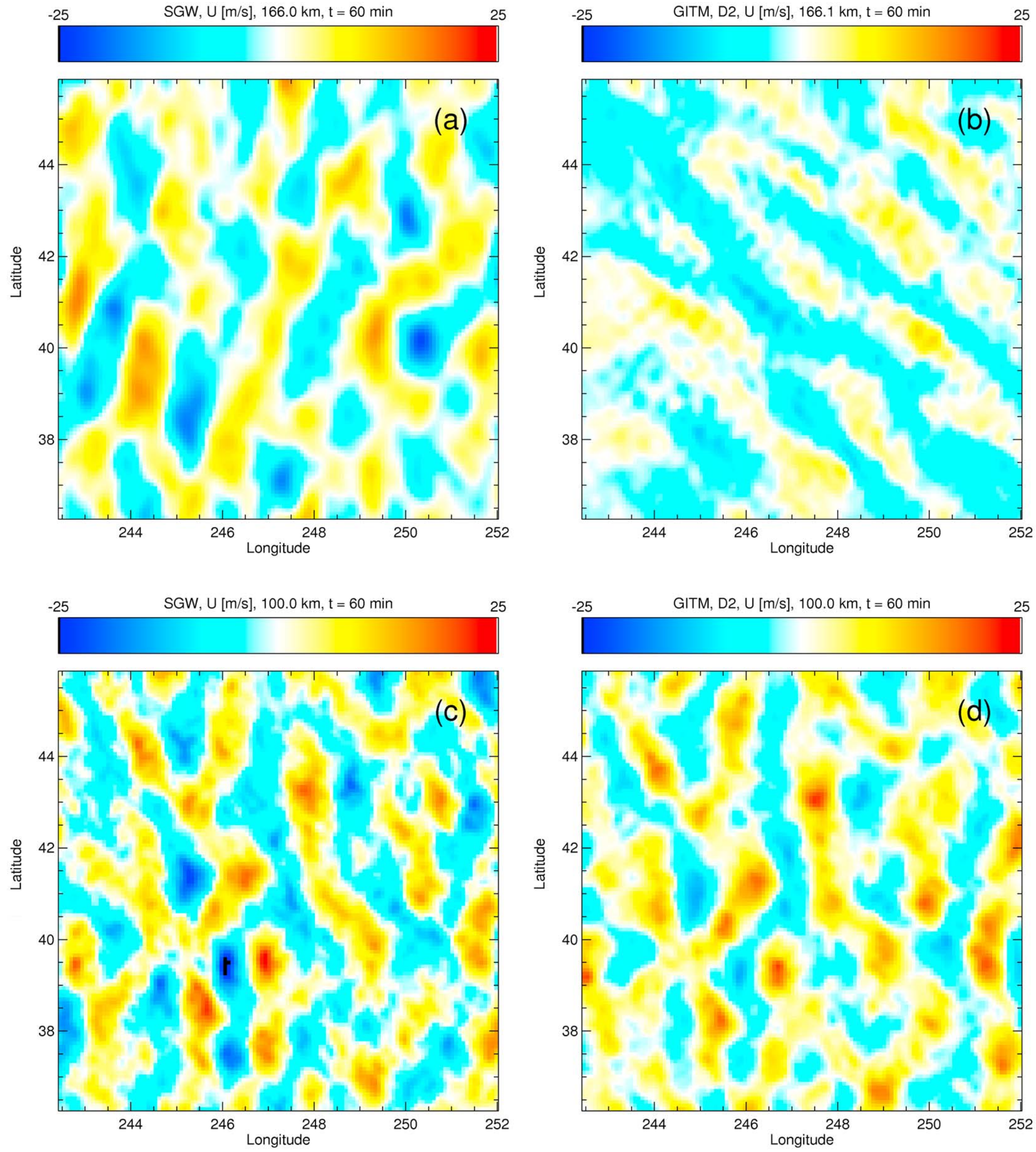

Figure 3. The zonal wind perturbation at (c and d) 100 km and (a and b) 170 km from the SGW model (Figures 3a and 3c) and from the GITM simulation (Figures 3b and 3d).

scope of this work, the physics within existing GW parameterization and ray-trace simulation to specific thermosphere momentum and body forcing—even accounting for winds, compressibility, molecular attenuation, etc—needs to be considered very carefully, and limitation of various approximations better understood in the future work.

2.3. Episodic Events

In order to further explore this first conclusion, we consider a north-south oriented TWP at the lower boundary of GITM from a hypothetical episodic event as the main feature shown in Figure 6. The TWP is a full-wavelength sinusoidal wave with a wavelength of 80 km, which is 10 times of the horizontal grid size. Although the wavelength can be less than 80 km, this value is selected so that the phase of waves and resulting IT response can be observed more clearly. The wave packet moves from west to east in the simulation domain with a constant speed and perturbs in zonal wind with a magnitude of ±16 m/s and in vertical wind with a magnitude of ±2 m/s. Calculation from the analytical model [*Meng et al.*, 2015] shows that these

Table 1. Magnitudes of the TWP and SGW Forcing

	SGW			TWP		
Setting[a]	U	V	W	U	W	v_p
MM-GW	±25 m/s	±25 m/s	±8 m/s	±16 m/s	±2 m/s	200 m/s
MM-AW	±25 m/s	±25 m/s	±8 m/s	±16 m/s	±2 m/s	800 m/s
LL-GW	±10 m/s	±10 m/s	±2 m/s	±8 m/s	±1 m/s	200 m/s
LL-AW	±10 m/s	±10 m/s	±2 m/s	±8 m/s	±1 m/s	800 m/s
ML-GW	±25 m/s	±25 m/s	±8 m/s	±8 m/s	±1 m/s	200 m/s

[a]The first letter for SGW level (L: low; M: moderate), the second letter for TWP level (L: low; M: moderate), GW for gravity waves, and AW for acoustic waves.

magnitudes of perturbation resemble a strong tsunami source. As the wave packet moves, it interacts with local air parcels and triggers the perturbation propagating upward into upper atmosphere. Phase speed and horizontal wave number of the TWP determine the frequency of the wave according to the polarization relations, through which perturbation amplitudes of different variables are related to one another [*Fritts and Alexander*, 2003; *Vadas and Fritts*, 2005; *Vadas and Nicolls*, 2012]. We present two cases in which the TWP travels at 200 m/s and 800 m/s from west to east. It roughly takes the slower TWP the entire simulation period (~60 min) to travel across the simulation domain while only ~15 min for the faster TWP. To the atmospheric layer directly in contact with the TWP, the TWP at 200 m/s induces waves of 2.5 mHz (6.7 min) and the one at 800 m/s induces waves of 10 mHz (1.7 min). From the background atmosphere, we obtain the buoyancy frequency of 4.5 mHz (3.7 min) and the acoustic cutoff frequency of 3.7 mHz (4.5 min) for the local condition and confirm that the former wave falls into GW branch and the latter into AW branch. Hereafter, we will simply refer these two cases as GWs and AWs (or TWP-GW and TWP-AW in the figures). The configurations are categorized as MM-GW and MM-AW in Table 1. We also obtain quantitative results for cases at three other configurations at different levels of wave activities.

3. Results

The simulation is performed around the UTTR site at 1–2 P.M. local time (20:00–21:00 UT) on 11 June 2007. GITM simulation starts at 24 h prior to the event onset. The bottom forcing starts 1 min into the 1 h event window, to simplify, at $t = 1$ min. The forcing gradually increases from zero to full magnitude within 5 min, and it is achieved by using a half cycle of sinusoidal function as the envelope.

Table 2 illustrates four scenarios of simulation settings used in this study. Scenario 1 setting is a controlled case with no additional bottom forcing. A TWP is introduced as an episodic event in the Scenario 2 runs. Scenario 3 setting studies ubiquitously present background wave activities that result from lower atmospheric disturbances and are characterized by SGW. TWP and SGW are implemented concurrently in the Scenario 4 runs. The differential fields of the IT variables among different simulation scenarios indicate the IT effects primarily resulting from a certain type of forcing. As listed in Table 3, when compared against the T3 controlled run, the differential fields, D1–D3, present the results by the forcing from TWP (Scenario 2−Scenario 1), SGW (Scenario 3–Scenario 1), and TWP + SGW (Scenario 4–Scenario 1). D4 is Scenario 4–Scenario 3. Both D1 and D4 present the TWP effects as the main contributor to the IT disturbances, but D4, with the presence of SGW, includes the effect of both linear and nonlinear interaction between TWP and SGW. Taking the difference of D4 and D1, hereafter *double differencing* or DD, therefore reveals the linear and nonlinear effects of interactions between the two types of forcing.

Table 2. Scenarios of Simulation Settings

Scenario	Traveling Wave Packet (TWP)	Stochastic Gravity Wavefield (SGW)
1	No	No
2	Yes	No
3	No	Yes
4	Yes	Yes

Table 3. Definition of the Differential Fields Presented in the Paper

	Difference	Main Contributor(s)
D1	Scenario 2–Scenario 1	TWP
D2	Scenario 3–Scenario 1	SGW
D3	Scenario 4–Scenario 1	TWP + SGW
D4	Scenario 4–Scenario 3	TWP with the presence of SGW
DD	D4–D1	Nonlinear interaction among IT species owing to SGW

3.1. Acoustic Gravity Waves

In Scenario 2, we initiate two types of waves by having the eastward TWPs travel at different speeds: GWs with the slower TWP and AWs with the faster TWP. It takes the slower TWP about 60 min to travel across

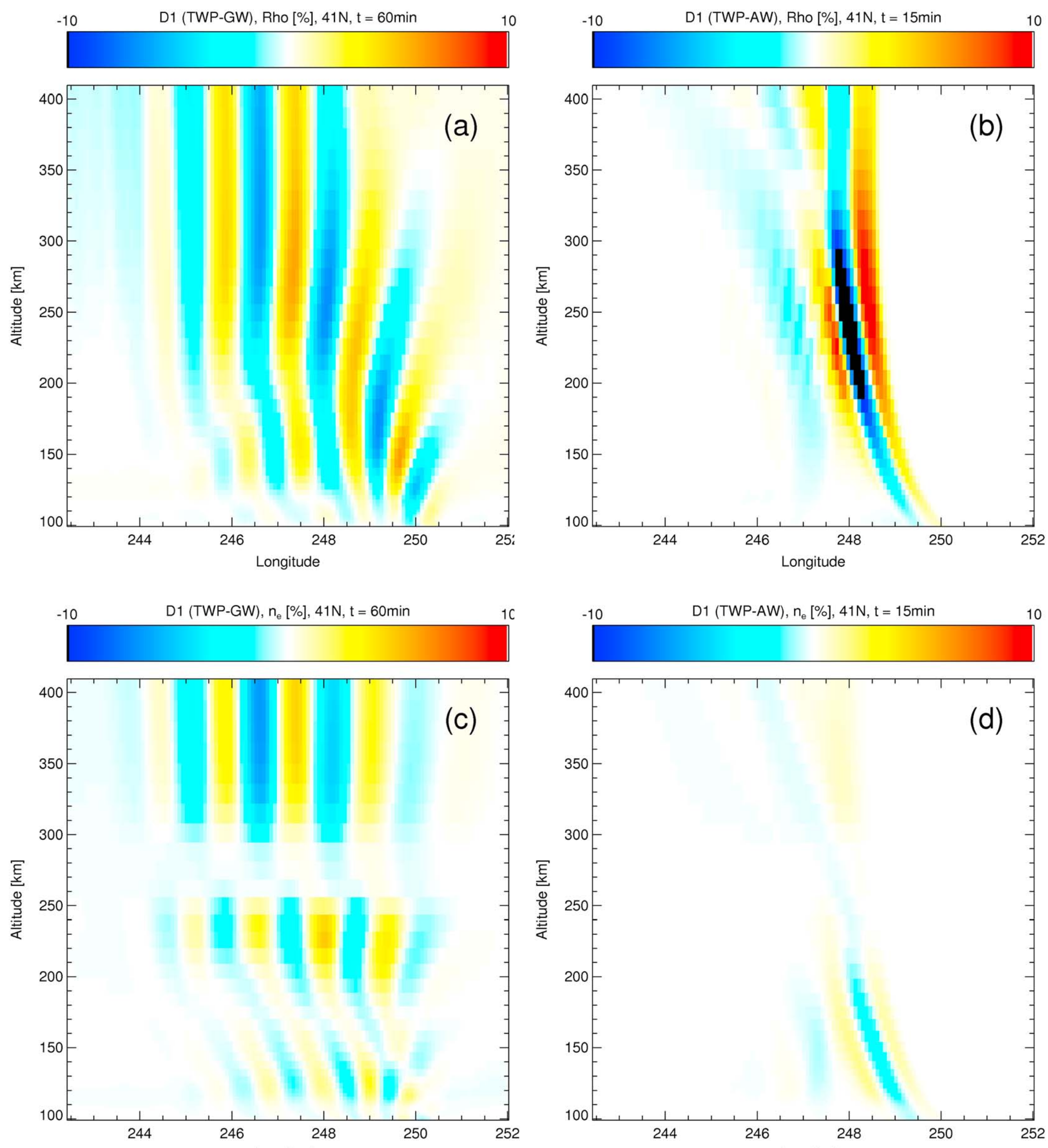

Figure 4. Altitude-longitude distribution of the perturbation, D1, in (a and b) neutral and (c and d) electron density to a TWP traveling eastward at 200 m/s (Figures 4a and 4c) and at 800 m/s (Figures 4b and 4d).

10.1002/2016JA022930

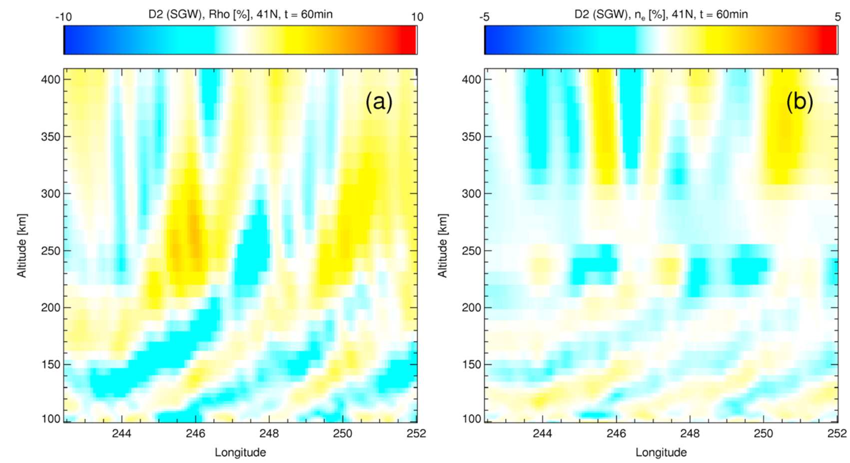

Figure 5. Altitude-longitude distribution of the (a) neutral and (b) electron density perturbation caused by the SGW, D2, at 41° N at $t = 60$ min.

the simulation domain and 15 min for the faster TWP. Figure 4 shows the altitude-longitude snapshots of the IT response when the TWPs approximately reach 250°E in both cases. The differential fields, D1, of neutral mass (Figures 4a and 4b) and electron number density (Figures 4c and 4d) have been shown. The wave patterns are clearly different between the GWs (Figures 4a and 4c) and AWs (Figures 4b and 4d). Although the AWs can cause greater localized perturbation, such as $>$10% in Figure 4b, the energy propagates upward so fast that it does not influence local air parcels long enough to develop a full cycle of oscillation, i.e., becomes an acoustic pulse. The waves do not sustain after two localized peaks in the neutral atmosphere. The perturbation in electron density is about 10 times lower than that in the neutral. On the other hand, the GWs travel upward and result in strong wave activities across the lower thermosphere. The phase fronts of perturbations steepen with altitude (i.e., dramatically increase in vertical wavelength) as a result of increasing viscous dissipation there [*Hines*, 1968a] as observed in Figure 1 of the work by *Hickey et al*. [2010]. Though similar magnitude, different vertical variations are observed in neutral mass density and electron number density. While the resulting oscillation is in phase throughout the lower thermosphere as shown in Figure 4a, the developed waves in electron density is out of phase above and beneath the *F* layer peak at ~250 km (low solar irradiance and low geomagnetic condition result in a low *F* layer peak as shown in Figure 2) as shown in Figure 4c. At these altitudes, collision between neutral and ionized species becomes less frequent and their dynamics is governed by their own equations of motion as well as chemical reactions and displays charge-dependent behaviors. The wave structures observed in electron density in Figure 4c, thus, are the overall results of perturbed background atmospheric conditions, such as ion/electron temperature, neutral wind, and density. The sustained GWs are locally observable in the IT system throughout the rest of the simulation window, up to 60 min, after the TWP has passed the lower boundary.

3.2. Time-Varying Background Perturbations

Scenario 3 is carried out by using only the SGW fields as bottom forcing. Another important result is that medium-scale traveling ionospheric disturbances (TIDs) and traveling atmospheric disturbances (TADs) are developed as soon as the wave energy reaches local air parcels. In this case, the main phase propagates NE-ward. Figure 5 presents altitude-longitude snapshots of the IT response to the SGW forcing, D2 as defined in Table 2, in neutral mass density (Figure 5a) and electron number density (Figure 5b) at 41°N. Compared to the magnitudes in Figure 4, the SGW forcing of similar peak-to-peak variation causes about ±5% variation in neutral density and about ±3% in electron density. The atmospheric filtering of certain wave modes and the nonlinear wave interactions among different wave modes contributes to an overall lower magnitude of variation. The magnitude of percentage perturbation in neutral density is slightly higher than that in electron density. Similar to the results in Figure 4, although the SGW-induced wave patterns are more complex (resulting from multiple wave modes), the wave structures are mostly in phase in the neutral and out of phase in the electrons above and beneath the *F* layer peak at ~250 km as shown in Figure 5.

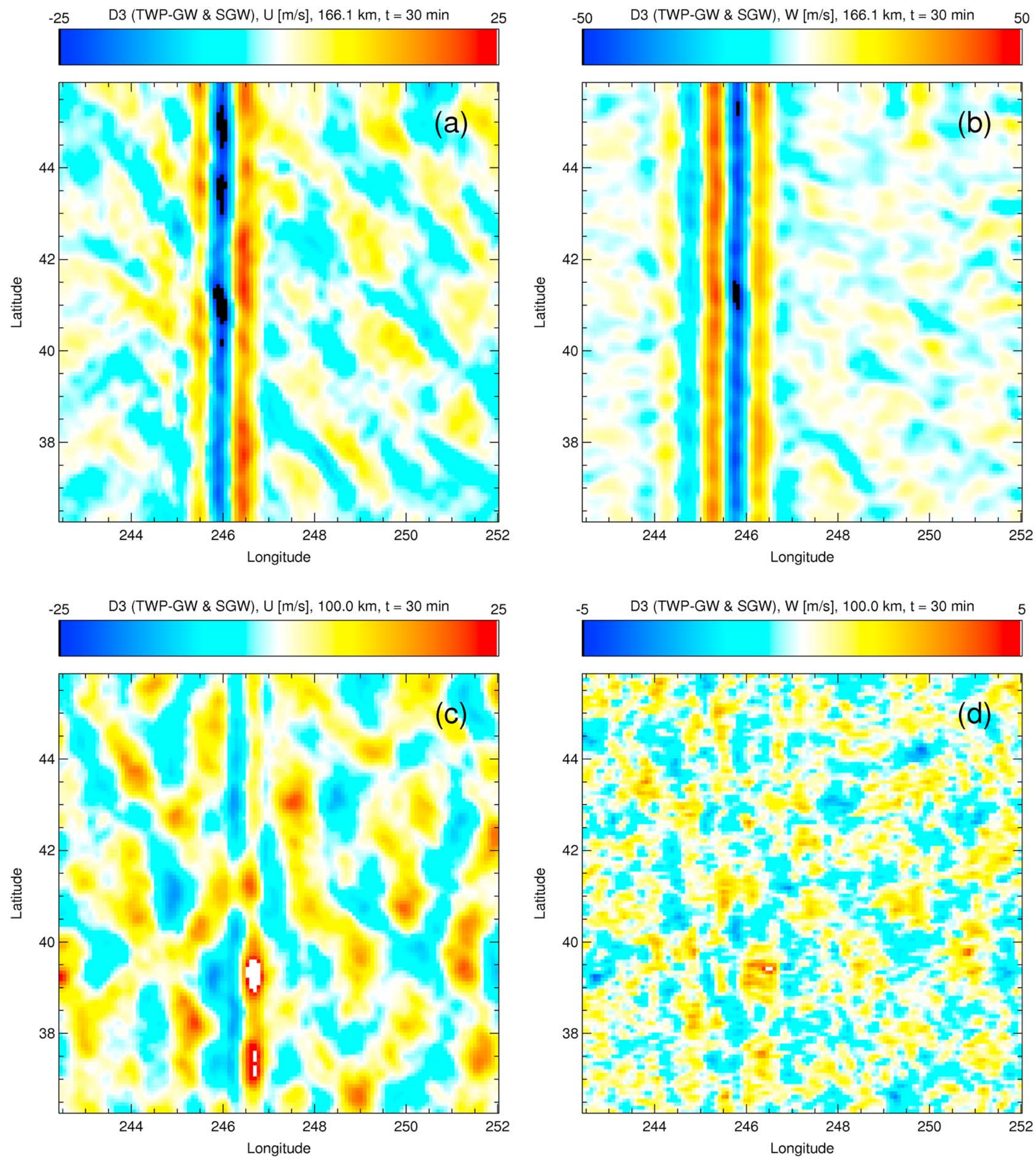

Figure 6. The differential fields in (a and c) zonal and (b and d) vertical winds at 170 km (Figures 6a and 6b) with the concurrent lower-boundary forcing from 100 km (Figures 6c and 6d).

We have observed slightly greater peak-to-peak variation in both neutral and electron density at the west half of the simulation domain when applying bottom forcing to the entire lower boundary. This phenomenon is also observable in Figure 5. The geophysical coordinates of (41°N, 243°E) and (41°N, 250°E) in the figure convert to 48.0°N and 49.2°N, respectively, in geomagnetic latitude. The tendency of a higher variation observed equatorward to the source is consistent with the recent observations [*Nishioka et al.*, 2013] and the 2-D modeling results for acoustic waves at low and middle latitudes [*Zettergren and Snively*, 2015].

3.3. Concurrent Episodic and Stochastic Forcing

Figure 6 illustrates the differential fields, D3, in zonal and vertical winds when both TWP and SGW are simul- **F6**
taneously present. Compared to D1, D3 includes the SGW field, which adds the complexity into the IT response, especially in the TWP-induced GW case as shown in Figure 7. Compared to the six distinct crests in Figure 4a, the vertical variation of the crests in Figure 7a appears to have more structures resulting from the ubiquitous SGW fields. For example, at the lower altitudes at around 244°E and at the higher altitudes at

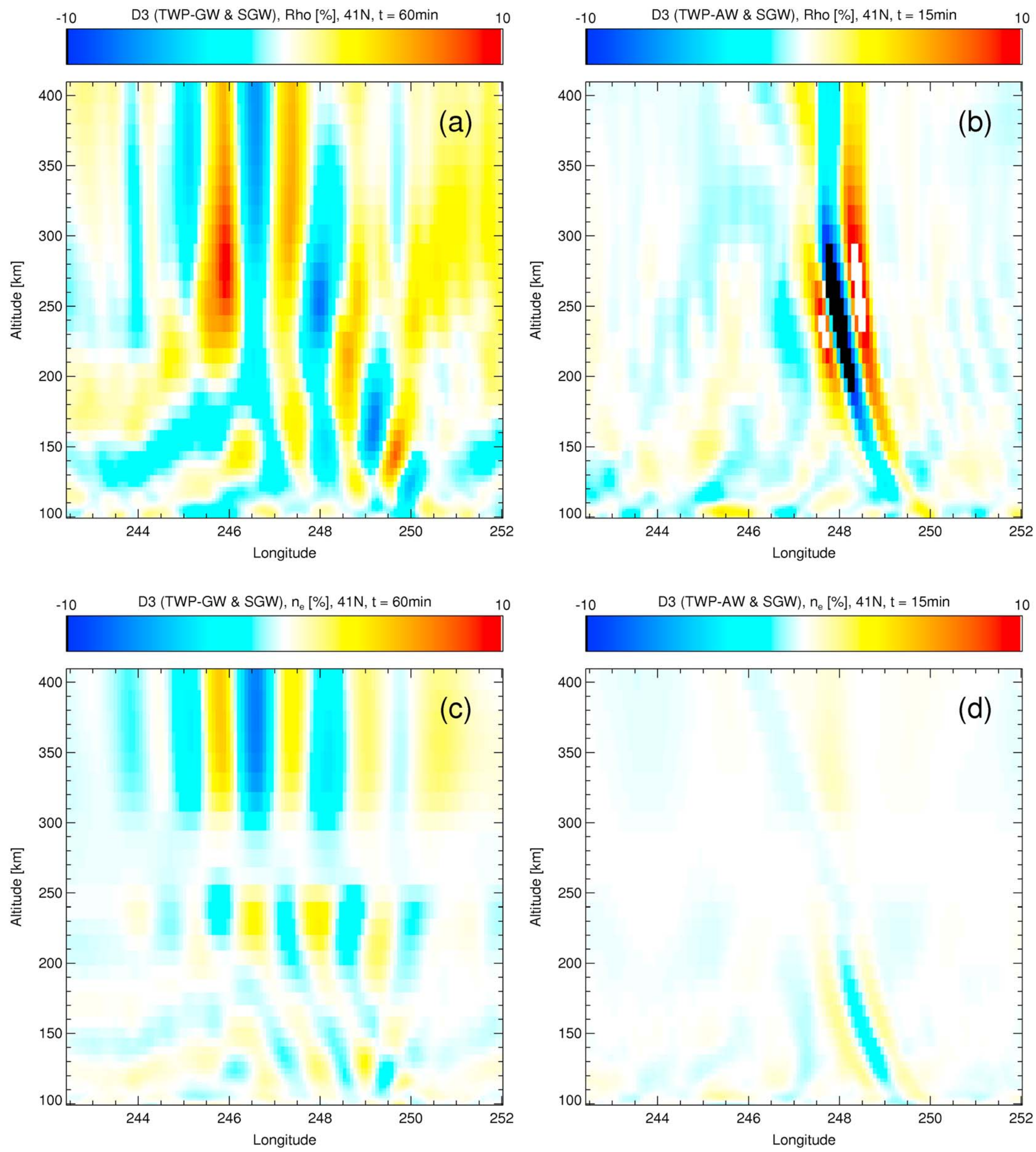

Figure 7. Altitude-longitude distribution of the IT response, D3, in (a and b) neutral and (c and d) electron to concurrent SGW and a TWP which travels eastward at 200 m/s (Figures 7a and 7c) and 800 m/s (Figures 7b and 7d) and induces GWs and AWs respectively.

around 251°E, more apparent wave activities appear in Figure 7a than in Figure 4a. The perturbation amplitudes and shapes of electron density at higher altitudes in Figure 7c are similar to those in Figure 4c, but patch-like structures fill up the bottom side of the ionosphere (100–200 km) in Figure 7c, which represent the consequence of wave-wave interaction between SGW and TWP. As a result of the fluctuation in electron density, the wavy structures modulated the total electron content (TEC) as shown in Figure 8a.

In Figures 7b and 7d, the TWP-induced AW case, the SGW effects are also presented but with lower magnitudes where further away from the major AW structures (compared to the GW case). The fluctuation in neutral and ionized atmosphere by the superposed SGW fields also appears not as strong as that in the D2 case as shown in Figure 5 when the SGW is the only forcing. For the purpose of comparison, the TWP-AW snapshots are taken at $t = 15$ min and the TWP-GW snapshots are taken at $t = 60$ min so that the TWP travels to the same lower boundary location in both cases. The atmosphere has only been under the full-magnitude SGW forcing

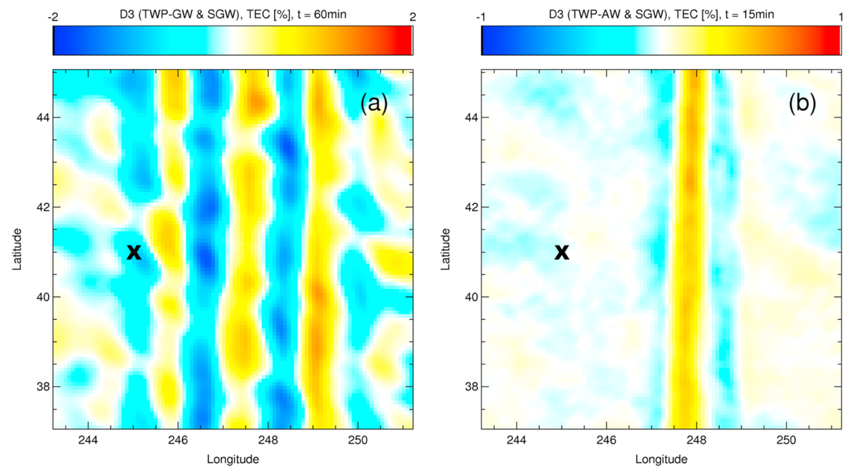

Figure 8. Latitude-longitude distribution of the IT response, D3, in TEC to concurrent SGW and a TWP traveling eastward at (a) 200 m/s and (b) 800 m/s. The crosses mark the location at (41°N, 245°E).

for 9 min whereas 54 min as in the GW cases (Figures 5 and 7a and 7c), slightly weaker perturbations thus seemingly appear. Similar to the results in Figures 4b and 4d, the fluctuation in electron density in Figure 7d is also much weaker than that in Figure 7b, the resulting peak-to-peak TEC variations therefore differ by about a factor of 4 as shown in Figure 8. The magnitudes of variation in the GW case are ±8.8% in neutral, ±6.2% in electron density, and ±1.5% in TEC. In the AW case, neutral density has stronger localized variation in neutral density (±13.9%) but overall lower variation in electron density (±2.1%) and TEC (±0.4%). Table 4 (MM-GW and MM-AW) summarizes the magnitude of IT variation observed in D3 for both types of waves. Note that the numbers listed in the table are the maximum perturbations observed from the differential fields over the entire domain of interest and do not necessarily imply a particular local air parcel undergoing such a magnitude of oscillation.

4. Discussions

4.1. Phase Speed and Wave Periods

Figure 9 shows the temporal variation of the altitudinal profiles of neutral and electron density perturbations at (41°N, 245°E), marked by crosses in Figure 8. A clear wave evolution of the IT response is present here. As the wave energy propagates upward, the direction of the phase propagation are clearly shown as downward for the GWs and upward for the AWs. In Figure 9a, the solid magenta arrow around 200 km indicates a downward phase speed of ~300 m/s from TWP-induced GWs as they develop nearly into deep horizontally propagating wave modes. In Figure 9b, the dotted blue arrow indicates an upward phase speed of ~900 m/s from TWP-induced AWs and the solid magenta arrow at 150 km indicates downward propagating phases with a speed of ~30 m/s induced by SGW.

Table 4. The IT Response to the Concurrent TWP and SGW Forcing at the Maximally Perturbed Epoch ($t = 60$ min for GW; $t = 15$ min for AW)[a]

	Rho				[e−]				TEC			
Setting	D1	D3	D4	DD	D1	D3	D4	DD	D1	D3	D4	DD
MM-GW	±6.6%	±8.8%	±6.4%	±1.4%	±5.7%	±6.2%	±5.6%	±1.1%	±1.4%	±1.5%	±1.4%	±0.5%
ML-GW	±3.4%	±6.0%	±3.4%	±0.9%	±3.0%	±4.0%	±2.7%	±0.7%	±0.7%	±1.0%	±0.7%	±0.3%
LL-GW	±3.4%	±3.7%	±3.4%	±0.4%	±3.0%	±2.9%	±2.8%	±0.3%	±0.7%	±0.8%	±0.7%	±0.1%
MM-AW	±12.6%	±13.9%	±13.8%	±2.8%	±2.2%	±2.1%	±2.1%	±0.3%	±0.3%	±0.4%	±0.4%	±0.1%
LL-AW	±6.9%	±6.9%	±6.8%	±0.4%	±1.1%	±1.1%	±1.1%	±0.1%	±0.2%	±0.2%	±0.2%	±0.0%

[a]Peak-to-peak magnitude is approximately twice as the listed values. The forcing settings are tabulated in Table 1.

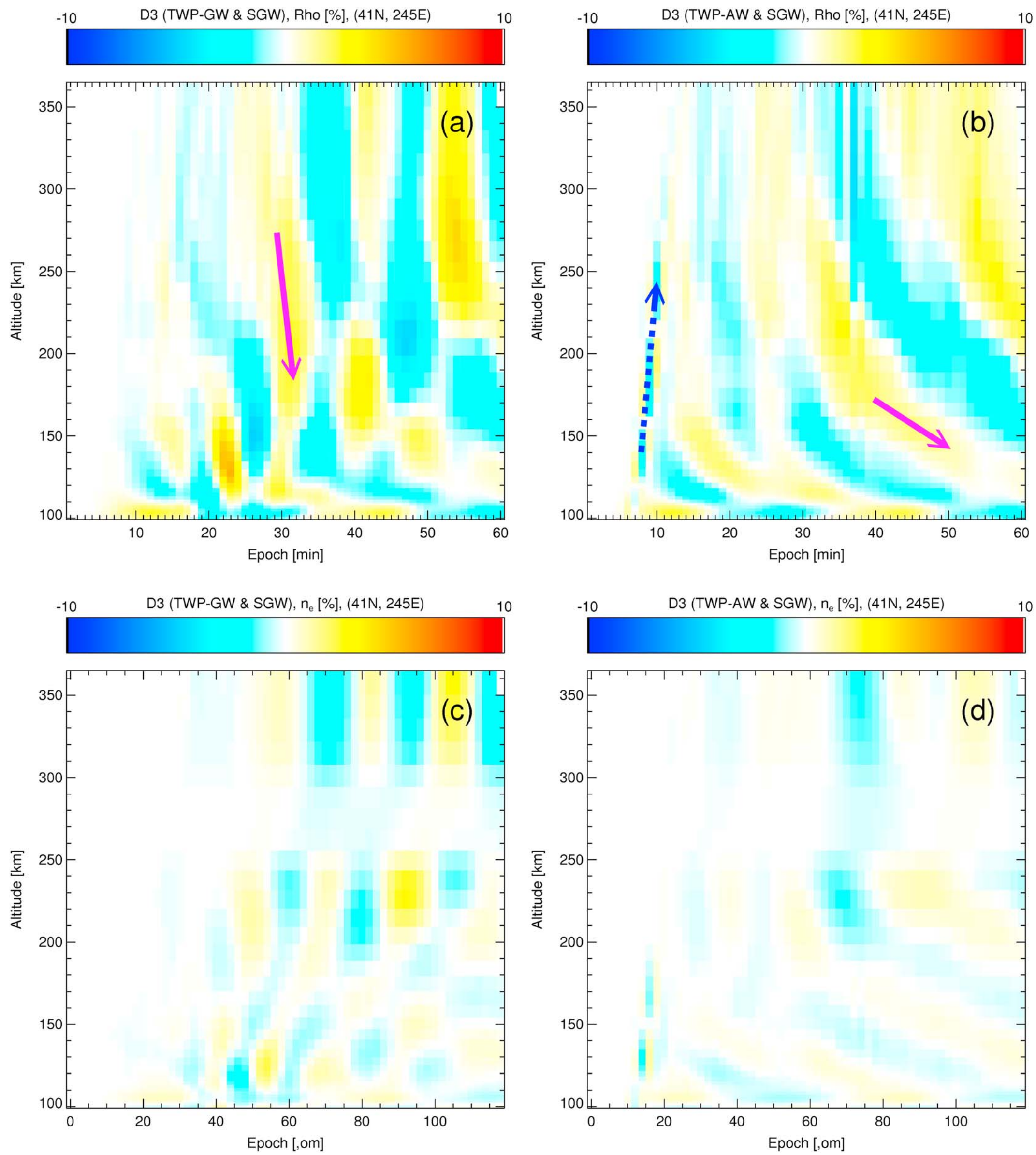

Figure 9. The evolution of altitudinal distribution of the IT response, D3, in (a and b) neutral and (c and d) electron density profiles at (41°N, 245°E), indicated by the Xs in Figure 7, to concurrent SGW and a TWP traveling eastward at 200 m/s (Figures 9a and 9c) and at 800 m/s (Figures 9b and 9d). In Figure 9a, the solid magenta arrow around 200 km indicates a downward phase speed of ~300 m/s from TWP-induced GWs. In Figure 9b, the dotted blue arrow indicates an upward phase speed of ~900 m/s from TWP-induced AWs and the solid magenta arrow at 150 km indicates downward propagating phases with a speed of ~30 m/s induced by SGW.

GWs experience dispersion and dissipation as they propagate upward in the thermosphere. As a consequence, wavelength broadening can be clearly observed as shown in Figure 4 for both TWP-induced GW and AW cases. Figure 10 examines the altitudinal distribution of the periodograms at 41°N, 245°E and shows how waves are progressively dispersed and dissipated. In Figure 10a the induced GWs have an extrinsic period of 6.7 min at 100 km and show a dominant period of 12 min above 200 km and most prominent near 250–300 km in neutral density. The results agree with the period of 12.3 min for upward propagating GWs at 250 km observed in simulation by *Vadas et al.* [2015]. The broadening of horizontal wavelengths owing to AW forcing has also been observed in TEC perturbations [*Zettergren and Snively*, 2015]. As wavelength broadening takes place in the TWP portion of spectrum (<15 min), as the result of scale-dependent dissipation, waves with longer horizontal wavelengths are more likely propagate into the upper thermosphere. In

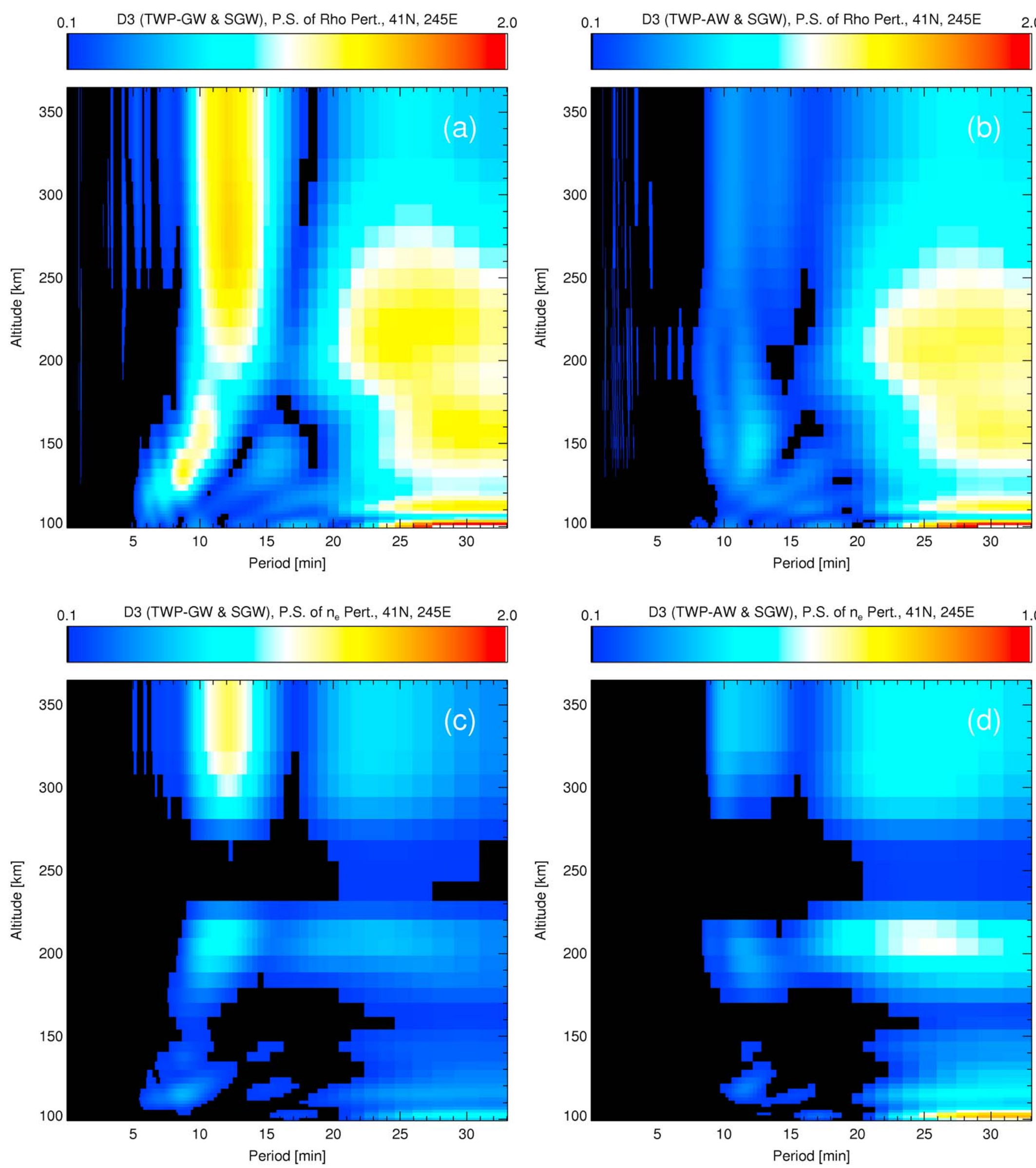

Figure 10. (a–d) Altitudinal distribution of periodogram of the D3 perturbation fields observed at (41°N, 245°E).

Figure 10c, the perturbation in electron density have similar dominant period in two distinct altitudinal regions around 210 km and above 270 km, which is below and above the *F* region density peak. Although the air parcels with direct contact to the TWP at the lower boundary are initially displaced at a single frequency, a spectrum of waves are developed when the energy propagates upward. On the other hand, the 4-times-faster TWP does not result in an apparent peak oscillation period at 3 min (one fourth of the dominant period for GWs) as expected in either Figures 10b or 10d. Mainly, the fact that the TWP travels away before it can establish a full-cycle oscillation to the local air parcels leads to transient disturbances and no apparent wave structures after the TWP passes.

The contribution of concurrent SGW forcing is deducible from comparison between the GW and AW cases and can be clearly observed from the nonzero power spectrum at longer periods (> ~17 min) in all the panels while some overlaps with the TWP effects at shorter periods. These features in periodicity appear similar among both the neutral (Figure 10a versus Figure 10b) and ionized (Figure 10c versus Figure 10d) atmosphere. The dominant features in the SGW-only forced spectrum show a tendency toward shorter periods

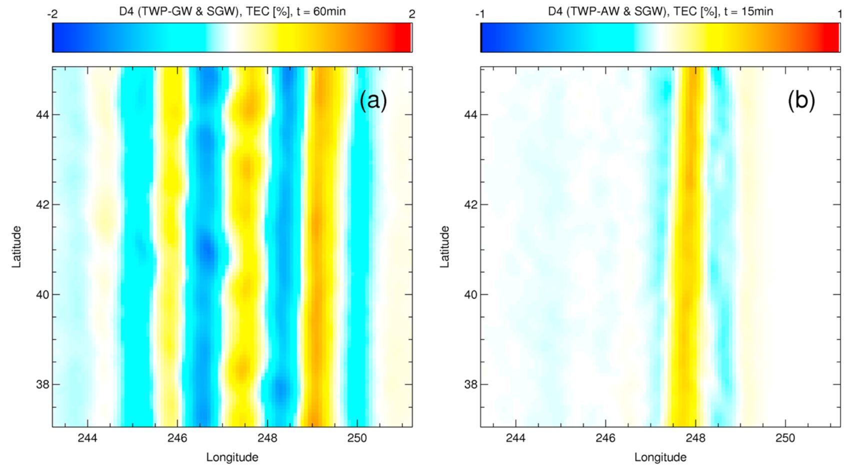

Figure 11. The IT response in TEC, D4, to a TWP traveling eastward (a and c) at 200 m/s and (b and d) at 800 m/s with the presence of SGW. After the perturbation caused by SGW is modeled and properly accounted for, the magnitude of D4 TEC perturbation lowers from that of D3. The induced wave patterns from the TWP present more distinctly compared to Figure 7 though the wave activities caused by SGW are still observable.

with altitude. This can be explained as the effect of preferential dissipation of the waves with shorter wavelengths that are associated with longer periods [*Walterscheid*, 2013].

4.2. Consideration of SGW

The atmosphere is scarcely steady and constantly experiences turbulence and disturbances. Wave patterns or structures that have been observed in TIDs and TADs in the recent studies [*Liu et al*., 2001; *Nishioka et al*., 2013; *Occhipinti et al*., 2006; *Tsugawa et al*., 2011] often result from but not exclusively owing to a single episodic event. Episodic perturbations under a completely quiet background atmosphere like the case study in section 3.1 is expected to be an exception, rather than the status quo. Rather, it is reasonable to expect that a major episodic event, such as volcano eruption or an earthquake, occurs under some degree of background activities as the case in section 3.3. A common practice of studying TEC variations is subtracting the smoothed preevent values from the event measurements. Table 3 lists various differential fields that we have studied. For practical applications, with prior knowledge or assumption of background activities, we can take D4 (Scenario 4–Scenario 3) instead of D3 (Scenario 4–Scenario 1) to illustrate the effects of TWP on the upper atmosphere with a turbulent lower atmosphere. Taking the D4 type of comparison in TEC (Figure 11), for example, it not only removes part of the wave structures contributed by the SGW perturbation fields but also brings down the peak-to-peak variation closer to the impact brought by the TWP only. Figure 12 shows the power spectra of the wave patterns in the differential fields of TEC variations: D1 (Figure 12a), D3 (Figure 12b), D4 (Figure 12c), and DD (Figure 12d). The horizontal wave numbers are given in the unit of km^{-1} instead of the conventional around-the-globe presentation regarding waves in the GCMs. For example, a wave number of 100 in the work by *Liu et al*. [2014] is equivalent to 0.003 km^{-1} (wavelength of ~400 km at the equator). In Figure 12a, the peak is centered at zonal wave number of 0.007 km^{-1}, which is equivalent to a wavelength of ~140 km. This dominant wavelength is longer than the TWP wavelength and can be attributed to the asymmetric nature of the TEC perturbation [*Hickey et al*., 2010; *Zettergren and Snively*, 2015]. No apparent meridional wave structures have developed. In Figure 12b, a group of nonzero zonal and meridional wave numbers with comparable magnitudes is attributable to the concurrent SGW forcing. By subtracting off variation caused by the SGW forcing (Scenario 3), we successfully decrease the “spread-out” of the wave number distribution as shown in Figure 12c. We expect to devote further modeling efforts to explore applications and make this feature available to potentially assist in better detection of TIDs and TADs.

4.3. Atmospheric Nonlinearity

As mentioned in section 2, it is assumed that the differential fields reveal the linear and nonlinear effects arising from the interaction between the TWP and SGW fields. As tabulated in Table 2, D1 shows the variation

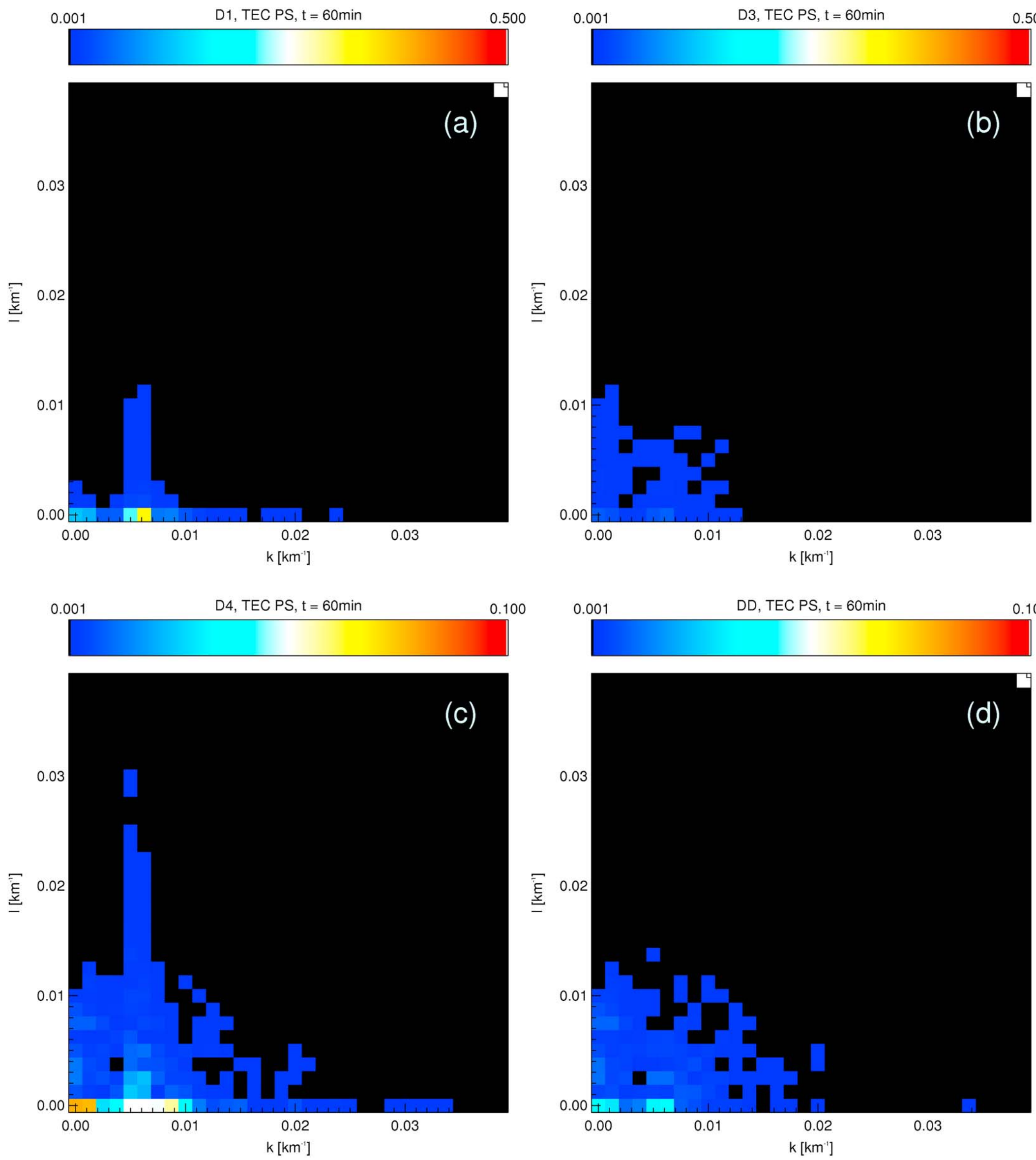

Figure 12. (a–d) The power spectra of four TEC differential fields. Note that the horizontal wave numbers are given in the unit of km^{-1} instead of the conventional around-the-globe presentation in the GCMs.

caused by TWP forcing and D4 shows that by concurrent TWP and SGW forcing. We define DD, the difference of D1 and D4, to analyze the impact resulting from the SGW forcing. If the atmosphere were a linear system, then D1 and D4 would have theoretically been identical because the SGW-caused variation, D2, would have been completely eliminated in D4. The facts that the atmosphere is hardly linear and that interactions between waves (primary effects to the observed variation) and other dynamic and chemical processes (secondary effects) exist result in the complex, nonuniform, and nonzero DD fields as shown in Figure 13. Note that the color bar ranges here are much smaller than those in Figures 4 and 7. The variation caused by either GWs or AWs can clearly be observed as the TWP propagates eastward. In Figure 13a, the lower lobe at the right-hand side and the elongated lobe at the left-hand side are similar to the ones in Figure 4a (D1, TWP-GW). On the other hand, the curvatures of the wavefronts here are modulated by those in Figure 5a (D2, SGW). As SGW contains GWs of various frequency and wavelengths, the DD field is not in phase with a particular differential field. The same phenomenon is also observable in the other panels. The power spectrum resulting from the SGW-TWP interaction shown in Figure 12d contains two peaks in the longitudinal wave numbers as traces left by the TWP and a continuum of lower power by the SGW. These components can

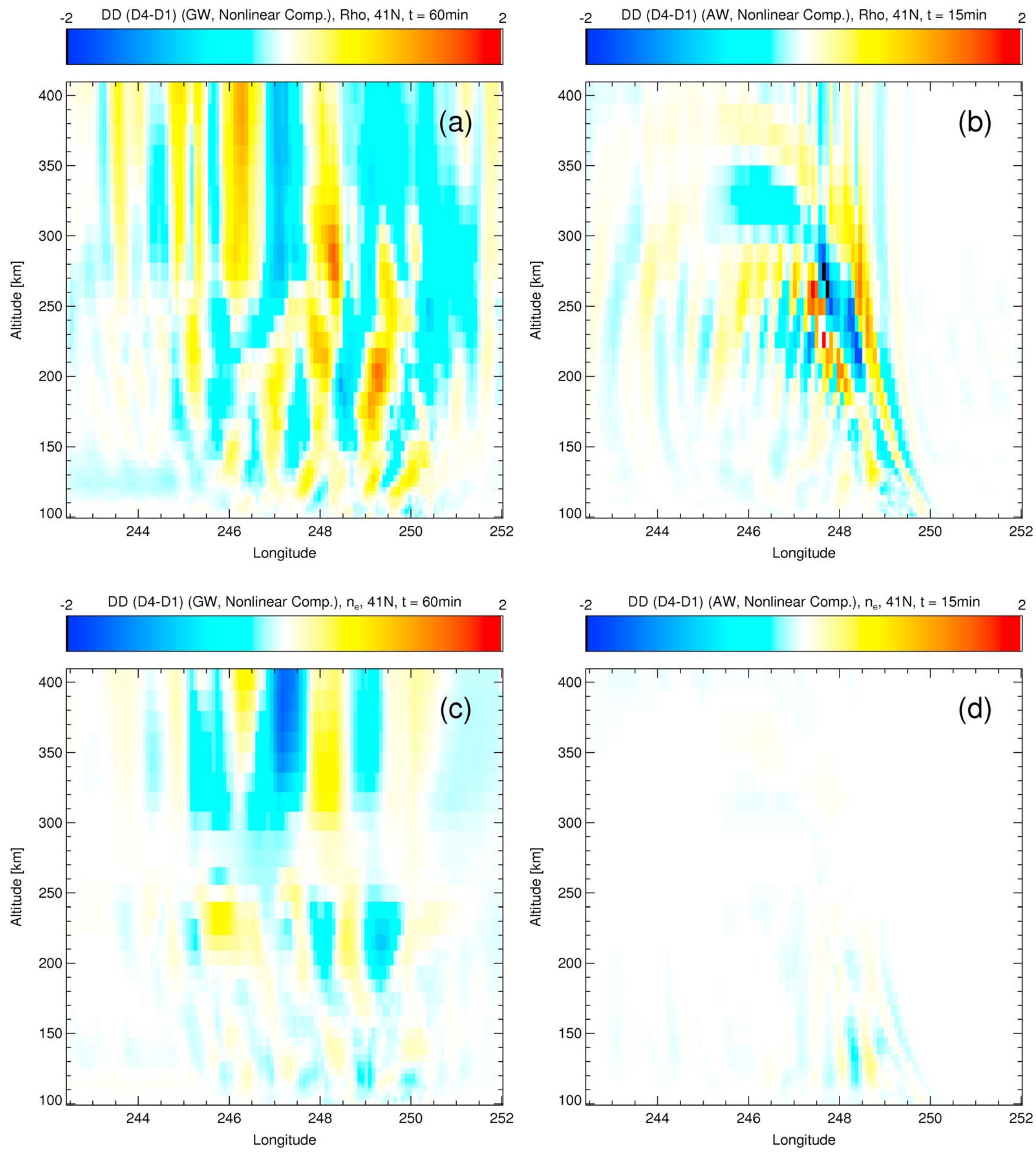

Figure 13. Altitude-longitude snapshots of the nonlinear component at 41°N in (a and b) neutral and (c and d) electron density owing to the interaction between SGW and TWP forcing.

be further examined in TEC as shown in Figure 14 with the magnitude in the GW case being five times stronger and the region of impacts relatively confined in the AW case. The magnitudes of residual components of IT variation for both GWs and AWs have been summarized in Table 4 (MM-GW and MM-AW). There values are obtained when the atmosphere is most perturbed in the simulation: $t = 60$ min for GWs and $t = 15$ min for AWs, the epochs that the TWP passes the same lower boundary location.

In order to better understand the wave-wave interactions in the IT, we alternate combinations of SGW activity levels and TWP strength as shown in Table 1 and perform the same analysis detailed in section 3 on these cases. Table 4 summaries the D1, D3, D4, and DD variations of neutral mass density, electron number density, and TEC. Higher SGW levels tend to lead to higher contribution from wave-wave interactions contribute up to 2.8% of the perturbations for the scenarios carried out in this study. However, in most cases the perturbation level is brought down to TWP-only level when the SGW effects are properly accounted for. It is worth noting that this is also true in a particular case (ML-GW) when the SGW forcing overwhelms a weak tsunami-like TWP.

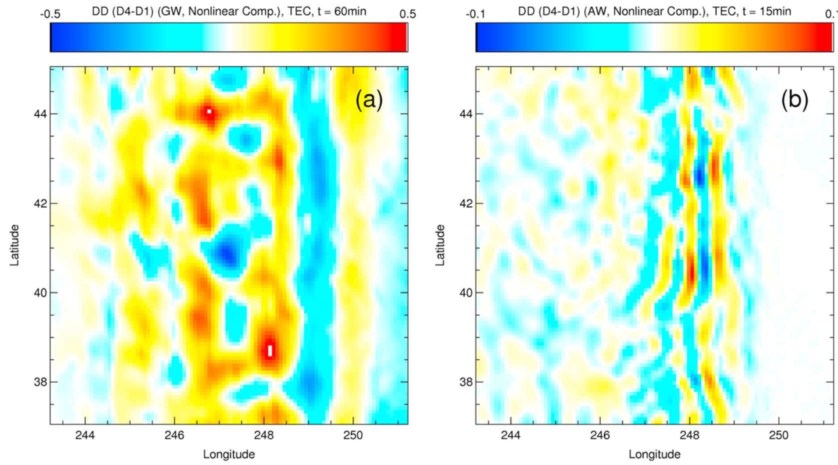

Figure 14. (a and b) The nonlinear component in TEC owing to the interaction between SGW and TWP forcing.

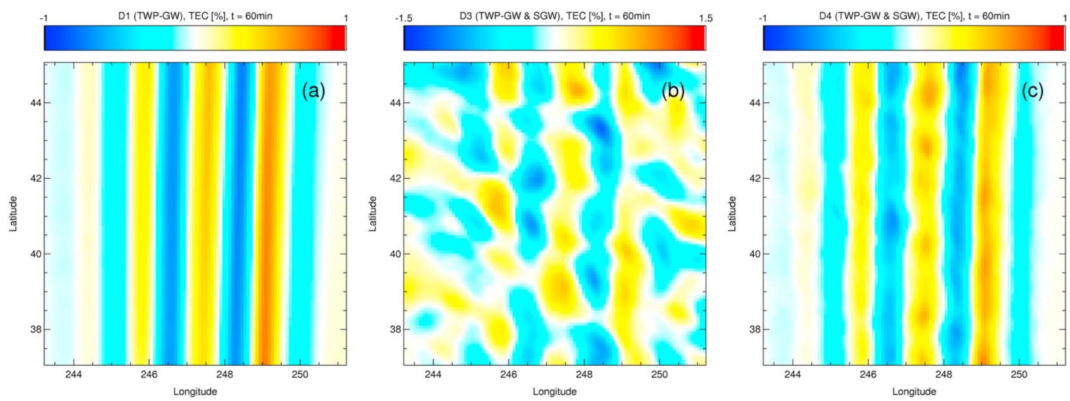

Figure 15. (a–c) The main TWP-induced perturbation patterns are obtained even in the case that the SGW forcing is much greater than the TWP forcing.

The comparison of D1, D3, and D4 of the ML-GW case is shown in Figure 15, where a distinct improvement is obtained as a result of knowledge of the SGW-introduced perturbations. A separate test has also been performed with overlapping TWP and SGW spectral components, and the isolated D4 field still contains clear TWP features with our approach (results not shown). This is because the differencing performed in the current study is in spatial and temporal domains rather than frequency domain. This again suggests that a good understanding of background wave activities not only is critical to interpreting the observed TID and TAD measurements but also provides potential and improvement in retrieving these disturbances from noise-like observations. Both aspects help us gain significant understanding of AGW effects on the IT system regardless where episodic events originate from.

5. Summary and Conclusions

For the first time, a tsunami-like wave packet is modeled with background wavefields and the impacts to the IT system are examined in this paper. This is a critical step toward understanding not only the link between upper atmosphere and natural hazards but also the important link between the integrated effects of continuous GW forcing of the IT system from below. Specially, four simulation scenarios have been set up to investigate how the IT system responds to episodic and stochastic forcing from the lower atmosphere using a 3-D model, GITM, which solves for nonlinear thermodynamic equations without hydrostatic assumption. The episodic event is characterized by a TWP traveling eastward at the lower boundary of the simulation domain. With different traveling velocity, the TWP induces GWs and AWs. The stochastic forcing is specified by the

SGW model, which provides time-varying perturbations from a spectrum of small-scale GWs. The differential fields of simulation scenarios in neutral mass density, electron number density, and TEC quantitatively characterize the IT variations. When TWP and SGW forcing occurs concurrently, the induced GWs cause variation of ±8.8% in neutral, ±6.2% in electron density, and ±1.5% in TEC. The magnitudes decrease by 2.4%—for example, from ±8.8% (D3) to ±6.4% (D4)—when the SGW effects are simulated separately and subtracted. On the other hand, the induced AWs cause variation of ±13.9% in neutral, ±2.1% in electron density, and ±0.4% in TEC. Furthermore, both GWs sustain in the ionosphere and thermosphere tens of minutes after the TWP has passed through the lower atmosphere and develop clear TIDs and TADs. In the AW case, the TWP travels away before it can establish a full-cycle oscillation to air parcels. This leads to transient disturbances and no apparent wave structures after the TWP passes.

We derive the theoretical oscillation frequency and phase speed of the induced waves from the perturbed atmosphere. Particularly, in the GW case the theoretical local oscillation frequency agrees well with the observed dominant period of 12 min. The power spectra from the observable TEC show a peak centered at zonal wave number of 0.007 km^{-1}, which is equivalent to a wavelength of ~140 km. A certain degree of frequency broadening from the initially induced frequency is observed in the IT response to the bottom forcing.

We perform various combinations of SGW activity levels and TWP strength and provide quantitative results of the IT response (summarized in Table 4). Higher SGW levels tend to lead to greater importance for nonlinear interactions, and the nonlinear wave-wave interactions contribute up to 2.8% (Rho in the MM-AW case) of the perturbations for the scenarios carried out in this study. We demonstrate that the TWP-induced perturbation can be isolated even when the SGW forcing overwhelms a weak TWP using the method proposed. We conclude that a good understanding of background wave activities not only is critical to interpreting the observed TID and TAD measurements but also provides potential improvement in retrieving these disturbances from noise-like observations. Both aspects help us gain significant understanding of AGW effects on the IT system regardless where episodic events originate from.

Acknowledgments
This research at the University of Texas at Arlington was supported by NSF through grant ATM0955629, NASA through grants NNX13AD64G and NNX14AD46G, and AFOSR through award FA9550-16-1-0059 and MURI award FA9559-16-1-0364. Drob acknowledges support from the Chief of Naval Research through the NRL 6.1 Base Program and grant N0001414WX20599 from the Office of Naval Research, Basic Research Challenge (BRC), "Couplings–Ocean to Space or Ionospheric Drivers from Below." Please contact Cissi Ying-tsen Lin (incen@vt.edu) for the model outputs presented in this study.

References

Banks, P. M., and G. Kockarts (1973), *Aeronomy Part B*, Academic Press, Cambridge, Mass.

Bilitza, D., L.-A. McKinnell, B. Reinisch, and T. Fuller-Rowell (2011), The International Reference Ionosphere (IRI) today and in the future, *J. Geod.*, *85*, 909–920, doi:10.1007/s00190-010-0427-x.

Bowling, T., E. Calais, and J. S. Haase (2013), Detection and modelling of the ionospheric perturbation caused by a Space Shuttle launch using a network of ground-based Global Positioning System stations, *Geophys. J. Int.*, *192*(3), 1324–1331, doi:10.1093/gji/ggs101.

Broutman, D., J. W. Rottman, and S. D. Eckermann (2003), A simplified Fourier method for nonhydrostatic mountain waves, *J. Atmos. Sci.*, *60*, 2686–2696, doi:10.1175/1520-0469(2003)060<2686:ASFMFN>2.0.CO;2.

Broutman, D., S. D. Eckermann, and J. W. Rottman (2009), Practical application of two turning-point theory to mountain-wave transmission through a wind jet, *J. Atmos. Sci.*, *66*, 481–494, doi:10.1175/2008JAS2786.

Broutman, D., S. D. Eckermann, and D. P. Drob (2014), The partial reflection of tsunami-generated gravity waves, *J. Atmos. Sci.*, *71*, 3416–3426, doi:10.1175/JAS-D-13-0309.1.

Broutman, D., J. Ma, S. D. Eckermann, and J. Lindeman (2006), Fourier-ray modeling of transient trapped lee waves, *Mon. Weather Rev.*, *143*, 2849–2856, doi:10.1175/MWR3232.1.

Calais, E., and J. B. Minster (1996), GPS detection of ionospheric perturbations following a Space Shuttle ascent, *Geophys. Res. Lett.*, *15*, 1897–1900, doi:10.1029/96GL01256.

Calais, E., J. Bernard Minster, M. Hofton, and M. Hedlin (1998), Ionospheric signature of surface mine blasts from Global Positioning System measurements, *Geophys. J. Int.*, *132*, 191–202, doi:10.1046/j.1365-246x.1998.00438.x.

Dautermann, T., E. Calais, and G. S. Mattioli (2009a), Global Positioning System detection and energy estimation of the ionospheric wave caused by the 13 July 2003 explosion of the Soufrière Hills Volcano, Montserrat, *J. Geophys. Res.*, *114*, B02202, doi:10.1029/2008JB005722.

Dautermann, T., E. Calais, P. Lognonné, and G. S. Mattioli (2009b), Lithosphere–atmosphere–ionosphere coupling after the 2003 explosive eruption of the Soufriere Hills Volcano, *Montserrat. Geophys. J. Int.*, *179*, 1537–1546, doi:10.1111/j.1365-246X.2009.04390.x.

Deng, Y., and A. J. Ridley (2007), Possible reasons for underestimating Joule heating in global models: E field variability, spatial resolution, and vertical velocity, *J. Geophys. Res.*, *112*, A09308, doi:10.1029/2006JA012006.

Deng, Y., and A. J. Ridley (2014), Simulation of non-hydrostatic gravity wave propagation in the upper atmosphere, *Ann. Geophys.*, *32*, 443–447, doi:10.5194/angeo-32-443-2014.

Deng, Y., A. D. Richmond, A. J. Ridley, and H.-L. Liu (2008), Assessment of the non-hydrostatic effect on the upper atmosphere using a general circulation model (GCM), *Geophys. Res. Lett.*, *35*, L01104, doi:10.1029/2007GL032182.

Drob, D. P., D. Broutman, M. A. Hedlin, N. W. Winslow, and R. G. Gibson (2013), A method for specifying atmospheric gravity wavefields for long-range infrasound propagation calculations, *J. Geophys. Res. Atmos.*, *118*, 3933–3943, doi:10.1029/2012JD018077.

Drob, D. P., et al. (2015), An update to the Horizontal Wind Model (HWM): The quiet time thermosphere, *Earth Space Sci.*, *2*, 301–319, doi:10.1002/2014EA000089.

Frances, S. H. (1973), Acoustic-gravity modes and large-scale traveling ionospheric disturbances of a realistic dissipative atmosphere, *J. Geophys. Res.*, *78*, 2278–2301, doi:10.1029/JA078i013p02278.

Fritts, D. C., and M. J. Alexander (2003), Gravity wave dynamics and effects in the middle atmosphere, *Rev. Geophys.*, *41*(1), 1003, doi:10.1029/2001RG000106.

Galvan, D. A., A. Komjathy, M. P. Hickey, and A. J. Mannucci (2011), The 2009 Samoa and 2010 Chile tsunamis as observed in the ionosphere using GPS total electron content, *J. Geophys. Res.*, *116*, A06318, doi:10.1029/2010JA016204.

Galvan, D. A., A. Komjathy, M. P. Hickey, P. Stephens, J. Snively, Y. Tony Song, M. D. Butala, and A. J. Mannucci (2012), Ionospheric signatures of Tohoku-Oki tsunami of March 11, 2011: Model comparisons near the epicenter, *Radio Sci.*, *47*, RS4003, doi:10.1029/2012RS005023.

Hagan, M. E., A. Maute, R. G. Roble, A. D. Richmond, T. J. Immel, and S. L. England (2007), Connections between deep tropical clouds and the Earth's ionosphere, *Geophys. Res. Lett.*, *34*, L20109, doi:10.1029/2007GL030142.

Heale, C. J., and J. B. Snively (2015), Gravity wave propagation through a vertically and horizontally inhomogeneous background wind, *J. Geophys. Res. Atmos.*, *120*, 5931–5950, doi:10.1002/2015JD023505.

Heale, C. J., J. B. Snively, M. P. Hickey, and C. J. Ali (2014), Thermospheric dissipation of upward propagating gravity wave packets, *J. Geophys. Res. Space Physics*, *119*, 3857–3872, doi:10.1002/2013JA019387.

Hedlin, M. A. H., and D. P. Drob (2014), Statistical characterization of atmospheric gravity waves by seismoacoustic observations, *J. Geophys. Res. Atmos.*, *119*, 5345–5363, doi:10.1002/2013JD021304.

Hickey, M. P., R. L. Walterscheid, M. J. Taylor, W. Ward, G. Schubert, Q. Zhou, F. Garcia, M. C. Kelly, and G. G. Shepherd (1997), Numerical simulations of gravity waves imaged over Arecibo during the 10-day January 1993 campaign, *J. Geophys. Res.*, *102*(A6), 11,475–11,489, doi:10.1029/97JA00181.

Hickey, M. P., G. Schubert, and R. L. Walterscheid (2009), Propagation of tsunami-driven gravity waves into the thermosphere and ionosphere, *J. Geophys. Res.*, *114*, A08304, doi:10.1029/2009JA014105.

Hickey, M. P., R. L. Walterscheid, and G. Schubert (2010), Wave mean flow interactions in the thermosphere induced by a major tsunami, *J. Geophys. Res.*, *115*, A09309, doi:10.1029/2009JA014927.

Hines, C. O. (1960), Internal atmospheric gravity waves at ionospheric heights, *Can. J. Phys.*, *38*(11), 1441–1481, doi:10.1139/p60-150.

Hines, C. O. (1967), On the nature of traveling ionospheric disturbances launched by low-altitude nuclear explosions, *J. Geophys. Res.*, *72*(7), 1877–1882, doi:10.1029/JZ072i007p01877.

Hines, C. O. (1968a), An effect of molecular dissipation in upper atmospheric gravity waves, *J. Atmos. Sol. Terr. Phys.*, *30*(5), 845–849, doi:10.1016/S0021-9169(68)80036-4.

Hines, C. O. (1968b), An effect of ohmic losses in upper atmospheric gravity waves, *J. Atmos. Sol. Terr. Phys.*, *30*(5), 851–856, doi:10.1016/S0021-9169(68)80037-6.

Huba, J. D., D. P. Drob, T.-W. Wu, and J. J. Makela (2015), Modeling the ionospheric impact of tsunami-driven gravity waves with SAMI3: Conjugate effects, *Geophys. Res. Lett.*, *42*, 5719–5726, doi:10.1002/2015GL064871.

Liu, H.-L., V. A. Yudin, and R. G. Roble (2013), Day-to-day ionospheric variability due to lower atmosphere perturbations, *Geophys. Res. Lett.*, *40*, 665–670, doi:10.1002/grl.50125.

Liu, H.-L., J. M. McInerney, S. Santos, P. H. Lauritzen, M. A. Taylor, and N. M. Pedatella (2014), Gravity waves simulated by high-resolution Whole Atmosphere Community Climate Model, *Geophys. Res. Lett.*, *41*, 9106–9112, doi:10.1002/2014GL062468.

Liu, J. Y., Y. I. Chen, Y. J. Chuo, and H. F. Tsai (2001), Variations of ionospheric total electron content during the Chi-Chi earthquake, *Geophys. Res. Lett.*, *28*, 1383–1386, doi:10.1029/2000GL012511.

Meng, X., A. Komjathy, O. P. Verkhoglyadova, Y.-M. Yang, Y. Deng, and A. J. Mannucci (2015), A new physics-based modeling approach for tsunami-ionosphere coupling, *Geophys. Res. Lett.*, *42*, 4736–4744, doi:10.1002/2015GL064610.

Nishioka, M., T. Tsugawa, M. Kubota, and M. Ishii (2013), Concentric waves and short-period oscillations observed in the ionosphere after the 2013 Moore EF5 tornado, *Geophys. Res. Lett.*, *40*, 5581–5586, doi:10.1002/2013GL057963.

Occhipinti, G., P. Lognonné, E. A. Kherani, and H. Hébert (2006), Three-dimensional waveform modeling of ionospheric signature induced by the 2004 Sumatra tsunami, *Geophys. Res. Lett.*, *33*, L20104, doi:10.1029/2006GL026865.

Perwitasari, S., T. Sakanoi, A. Yamazaki, Y. Otsuka, Y. Hozumi, Y. Akiya, A. Saito, K. Shiokawa, and S. Kawamura (2015), Coordinated airglow observations between IMAP/VISI and a ground-based all-sky imager on concentric gravity wave in the mesopause, *J. Geophys. Res. Space Physics*, *120*, 9706–9721, doi:10.1002/2015JA021424.

Picone, J. M., A. E. Hedin, D. P. Drob, and A. C. Aikin (2002), NRLMSISE-00 empirical model of the atmosphere: Statistical comparisons and scientific issues, *J. Geophys. Res.*, *107*(A12), 1468, doi:10.1029/2002JA009430.

Pitteway, M. L., and C. O. Hines (1963), Viscous damping of atmospheric gravity waves, *Can. J. Phys.*, *41*, 1935–1948, doi:10.1139/p63-194.

Rawer, K., D. Bilitza, and S. Ramakrishnan (1978), Goals and status of the International Reference Ionosphere, *Rev. Geophys.*, *16*, 177–181, doi:10.1029/RG016i002p00177.

Ridley, A. J., Y. Deng, and G. Tóth (2006), The global ionosphere-thermosphere model, *J. Atmos. Sol. Terr. Phys.*, *68*(8), 839–864, doi:10.1016/j.jastp.2006.01.008.

Saito, T., Y. Ito, D. Inazu, and R. Hino (2011), Tsunami source of the 2011 Tohoku-Oki earthquake, Japan: Inversion analysis based on dispersive tsunami simulations, *Geophys. Res. Lett.*, *38*, L00G19, doi:10.1029/2011GL049089.

Schunk, R., and A. Nagy (2009), *Ionospheres*, 2nd ed., Cambridge Univ. Press.

Semenov, A. O., and G. M. Shved (2008), Comparing parametrization of the coefficient of molecular thermal conductivity of the thermosphere, ISSN, *Geomagn. Aeron.*, *48*(6), 787–792, doi:10.1134/S001679320806011X.

Snively, J. B. (2013), Mesospheric hydroxyl airglow signatures of acoustic and gravity waves generated by transient tropospheric forcing, *Geophys. Res. Lett.*, *40*, 4533–4537, doi:10.1002/grl.50886.

Tsugawa, T., A. Saito, Y. Otsuka, M. Nishioka, T. Maruyama, H. Kato, T. Nagatsuma, and K. T. Murata (2011), Ionospheric disturbances detected by GPS total electron content observation after the 2011 off the Pacific coast of Tohoku Earthquake, *Earth Planets Space*, *63*, 875–879, doi:10.5047/eps.2011.06.035.

Vadas, S. L. (2013), Compressible f-plane solutions to body forces, heatings, and coolings, and application to the primary and secondary gravity waves generated by a deep convective plume, *J. Geophys. Res. Space Physics*, *118*, 2377–2397, doi:10.1002/jgra.50163.

Vadas, S. L., and D. C. Fritts (2005), Thermospheric responses to gravity waves: Influences of increasing viscosity and thermal diffusivity, *J. Geophys. Res.*, *110*, D15103, doi:10.1029/2004JD005574.

Vadas, S. L., and M. J. Nicolls (2012), The phases and amplitudes of gravity waves propagating and dissipating in the thermosphere: Theory, *J. Geophys. Res.*, *117*, A05322, doi:10.1029/2011JA017426.

Vadas, S. L., J. J. Makela, M. J. Nicolls, and R. F. Milliff (2015), Excitation of gravity waves by ocean surface wave packets: Upward propagation and reconstruction of the thermospheric gravity wave field, *J. Geophys. Res. Space Physics*, *120*, 9748–9780, doi:10.1002/2015JA021430.

Walterscheid, R. L. (2013), The propagation of transient wave packets in highly dissipative media, *J. Geophys. Res. Space Physics*, *118*, 878–884, doi:10.1002/jgra.50097.

Warner, C. D., and M. E. McIntyre (1996), On the propagation and dissipation of gravity wave spectra through a realistic middle atmosphere, *J. Atmos. Sci.*, *53*, 3213–3235, doi:10.1175/1520-0469(1996)053<3213:OTPADO>2.0.CO;2.

Warner, C. D., and M. E. McIntyre (2001), An ultrasimple spectral parameterization for nonorographic gravity waves, *J. Atmos. Sci.*, *58*, 1837–1857, doi:10.1175/1520-0469(2001)058<1837:AUSPFN>2.0.CO;2.

Yeh, K. C., and C. H. Liu (1974), Acoustic-gravity waves in the upper atmosphere, *Rev. Geophys.*, *12*(2), 193–216, doi:10.1029/RG012i002p00193.

Yue, J., B. Thurairajah, L. Hoffmann, J. Alexander, A. Chandran, M. J. Taylor, J. M. Russell III, C. E. Randall, and S. M. Bailey (2014), Concentric gravity waves in polar mesospheric clouds from the Cloud Imaging and Particle Size experiment, *J. Geophys. Res. Atmos.*, *119*, 5115–5127, doi:10.1002/2013JD021385.

Zettergren, M. D., and J. B. Snively (2013), Ionospheric signatures of acoustic waves generated by transient tropospheric forcing, *Geophys. Res. Lett.*, *40*, 5345–5349, doi:10.1002/2013GL058018.

Zettergren, M. D., and J. B. Snively (2015), Ionospheric response to infrasonic-acoustic waves generated by natural hazard events, *J. Geophys. Res. Space Physics*, *120*, 8002–8024, doi:10.1002/2015JA021116.